Enhancing the Photocatalytic Activity of TiO₂ by Modifying Surface with Polar Organic Anions for photocathodic Protection of 304 Stainless Steel

Zheng Ma[1,2,3,5], Xuehui Liu[1,4], Xiumin Ma[2,3,5], Lifei Wang[3,4,5], Baorong Hou[1, 2,3,5*]*

[1] Institute of Marine Science and Technology, Shandong University, No. 72 Binhai Road, Qingdao, 266237, P. R. China.
[2] Open Studio for Marine Corrosion and Protection, Pilot National Laboratory for Marine Science and Technology, No. 1 Wenhai Road, Qingdao, 266200, P. R. China.
[3] Institute of Oceanology, Chinese Academy of Sciences, No. 7 Nanhai Road, Qingdao, 266071, P. R. China.
[4] State Key Laboratory for Marine Corrosion and Protection, Luoyang Ship Material Institute, Qingdao, Shandong Province 266101, P.R. China
[5] Center for Ocean Mega-Science, Chinese Academy of Sciences, 7 Nanhai Road, Qingdao, 266071, P. R. China.
[*]E-mail: houbr@qdio.ac.cn

In this study, TiO₂ nanotube arrays (TiO₂ NTAs) were successfully prepared using 4-nitrothiophenol complex on the surface of fabricated arrays via the two-step anodization of Ti substrate, followed by a hydrothermal method. The formation of Ti–S band on the surface of TiO₂ NTAs increased the light absorption property of TiO₂. The existence of benzene ring and nitro increased the efficiency of hole transfer and further promoted the separation efficiency of photoinduced carriers in TiO₂ NTAs. Under visible light irradiation, the composite film demonstrated an effective photocathodic protection of 304 stainless steel.

1. INTRODUCTION

As water flows downhill, electrons automatically move from the negative potential to the positive one. When the smelted metal is placed in the environment, electrons will spontaneously transfer from the metal's body phase to the environment, and corrosion will occur. Corrosion has been a serious problem in people's life. According to relevant statistics, the annual corrosion loss accounts for about

3%–5% of each country's Gross Domestic Product (GDP) [1]. Corrosion protection is an urgent problem that needs to be solved.

The main purpose of corrosion protection is to keep electrons in the metal phase. The water in the lake continues to flow downstream without drying up because more and more water is being injected into the lake. Tracing back at the source, water in the lower reaches (e.g., ocean, river, and ground) evaporates into the air and becomes rain under the influence of solar energy and eventually flows into the lakes. The most permanent way to protect a metal is to find a "pump" that transfers electrons from a positive potential to a negative potential with the help of solar energy, and then injects them onto the surface of the metal. Yuan [2] coated copper with titanium dioxide and protected the copper under the light to prove that photocathodic protection is a feasible strategy in the field of metal protection [3-6].

As a new cathodic protection method, photocathodic protection has been widely examined by scholars because it does not consume power, and anode materials and has a theoretical permanent validity. However, this method also possesses several advantages that hinders its utilization, such as the following: (1) conductance potential of n-type semiconductors, (2) the pump should be more negative than the self-corrosion potential of metals in the environment, (3) high photoinduced carrier separation efficiency, and (4) high current requirement under sunlight exposure [7-10].

TiO_2 has been widely used in photocracking water and photodegrading organic pollutants and solar cells due to its excellent photoelectric properties and high-cost performance [11-13]. The conduction band (CB) of TiO_2 is more negative than the corrosion potential of 304 stainless steel (304 SS) in 3.5 wt.% NaCl solution. TiO_2 is a potential semiconductor material for photocathodic protection of 304 SS. TiO_2 nanotube arrays (TiO_2 NTAs) have been used by many researchers for photocathodic protection research. However, the balance of TiO_2 as an oxide semiconductor with d^0 electron configuration transition metal ions is composed of O 2P orbital. Consequently, TiO_2 can only absorb a small fraction of the UV light in the solar spectrum. Another defect of TiO_2 is the high recombination rate of photoinduced carriers. Therefore, TiO_2 cannot meet the requirements of 304 SS cathodic protection. At present, the strategies to expand the photo response of TiO_2 mainly include anion doping, LSPR effect, and narrow bandgap semiconductor loading. Moreover, the strategies to accelerate the carrier separation of TiO_2 mainly include the introduction of co-catalyst, construction of heterojunction composite, and regulation of semiconductor crystal face.

The modification using polar organic anions can be a good strategy to decrease the recombination rate of photoinduced carriers in TiO_2 [14-17]. The polar organic anions can be used as ligands to complex Ti (IV) on the surface of TiO_2, which changes the energetic position of surface states of TiO_2 and affect the intervention on photoinduced carrier transfer events. Organic ligands offer greater flexibility for surface modification than inorganic treatments due to the possibility of changing functional groups.

4-Nitrothiophenol is the preferred polar organic molecule for TiO_2 modification [18-22]. The •SH in 4-nitrothiophenol will react with •OH on the surface to form a Ti–S bond. The introduction of S changes the energy band structure on the surface of TiO_2 and causes the absorption edge to shift red.

In this study, TiO_2 NTAs have prepared through a two-step anodization process. The polar organic anions form a film on the surface of the TiO_2 NTAs through a hydrothermal method. The photoabsorption performance of TiO_2 NTAs is improved, and the photoinduced carrier coincidence rate

of TiO_2 NTAs is reduced. The electrochemical test shows that the modified TiO_2 NTAs has a satisfactory photocathodic protection effect on 304 SS.

2. EXPERIMENT

2.1 Reagents

The reagents involved in this study were purchased and used directly without any purification. NH_4F, $(CH_2OH)_2$, Na_2S, and C_3H_7NO were obtained from Sinopharm Chemical Reagent Co., Ltd.; 4-NO_2–C_6H_6SH was purchased from Tokyo Chemical Industry Co., Ltd.; 304 SS (10.0 mm × 10.0 mm) was purchased from Yangxin Shengxin Technology Development Co., Ltd.; and the H-type photochemical electrolytic cell is custom-made by Tianjin AIDA HENGSHENG Technology Development Co., Ltd.

2.2 Preparation of TiO_2 NTAs and 4NBT–TiO_2 NTAs

A two-step anodization process [23-24] was performed to fabricate the TiO2 NTAs. The Ti sheet (99.9%) with a thickness of 0.25 mm was cut into 10.0 mm × 30.0 mm foils and ultrasonically washed with ethanol, acetone, and deionized water for 15 min in sequence before setting aside. The NH_4F solution (1.72 g) was dissolved in 50.0 mL deionized water. Then, 450.0 mL $(CH_2OH)_2$ was added and stirred until the solution became uniform. In the two-step anodization process, the flat Ti foil was used as the anode, the Pt foil as the cathode, and the NH_4F solution as the electrolyte. The first step of the anodic oxidation process lasted for 1 h. The oxidized Ti foils were ultrasonically cleaned in 1 M HCl aqueous solution to remove the impurities and irregular nanotubes on the surface. Similarly, the second step of the anodic oxidation process took 1 h. The oxidized Ti foils were rinsed with deionized water, dried, and calcined in a muffle oven at 450 °C for 2 h to produce the TiO_2 NTAs.

The composites consisting of the polar organic molecule coating on the TiO_2 NTAs were achieved through a facile hydrothermal reaction. Approximately 1.33 mmol of polar organic molecule 4-NO_2–C_6H_6SH was dispersed into 30.0 mL of deionized water, and 10.0 mL C_3H_7NO was added. When the 4-nitrothiophenol was fully dissolved, the solution was transferred to a 50.0 mL SS Teflon-lined autoclave, wherein the anodized TiO_2 NTAs were placed at the bottom. The autoclave was kept at 120.0 °C for 24 h, and the TiO_2 NTA composite taken from the autoclave was rinsed with ethanol and deionized water in turn. The composites were prepared and labeled 4NBT–TiO_2 NTAs.

2.3 Material characterization

The crystal structure of NTAs was determined by X-ray diffraction (XRD) over the scan range of 10°-80° using a Bruker D8 Advance diffractometer at a scan rate of 6 degree/min with high-intensity Cu Kα radiation (I λ = 0.154 nm). The morphology of the synthesized samples was investigated on Hitachi S-4800 (Japan) via field emission scanning electron microscope (SEM). X-ray photoelectron

spectroscopy (XPS) was performed with an ESCALAB 250 Xi commercial instrument (Thermo Fisher Scientific, Al-Kα radiation, 1486.6 eV), with a C 1s photoelectron peak (binding energy at 284.6 eV) as energy reference. The UV-vis diffuse reflectance spectra (DRS) of the samples were measured on a Shimadzu UV 2550 spectrophotometer with an integrating sphere. Fourier transform infrared spectroscopy (FTIR) analysis was performed using a Shimazduo UV 2550 Fourier infrared spectrophotometer. The photoluminescence (PL) spectra of the synthesized samples were measured using an Edinburgh Instruments F-4500 fluorescence spectrometer with $BaSO_4$ as the reference sample. The electrochemical and photoelectrochemical experiments were implemented using a Chi 660E electrochemical workstation.

2.4 Photoelectrochemical measurements

A 304 electrode was fabricated by sealing the 304 SS into epoxy, leaving an exposed area of 1.0 $\times$ 1.0 cm^2. Photoanodes (TiO_2 electrode and 4NBT- TiO_2 electrode) were made from the prepared semiconductor materials and sealed with room-temperature vulcanized 704 silicone rubber to give a consistent exposed area.

The photocathodic protection performance properties were evaluated through the photoinduced variations of the open circuit potentials, variations of the photoinduced current density, and Potentiodynamic polarization curves. The photoinduced variations of the open circuit potentials and variations of the photoinduced current density curve was realized in an H-type electrolytic cell with a Xe lamp (PLS-SXE 300C, Beijing Perfect Light Company, China). The lamp equipped with a 420-nm UV-cut filter was utilized as the irradiation source. The electrolyte in the photoelectric cell of the H-type electrolytic cell was composed of 0.25M Na_2S and 0.35M Na_2SO_3, whereas that in the corrosion cell was composed of 3.5wt.% NaCl solution. The I–V curve was realized in a three-electrode system with the prepared 4NBT–TiO_2 NTAs as the working electrode, Pt foil as the counter electrode, saturated calomel electrode (SCE) as the reference electrode, and 0.25M Na_2S and 0.35M Na_2SO_3 as the electrolyte.

3. RESULTS AND DISCUSSION

The XRD patterns of the as-prepared TiO_2 and 4NBT–TiO_2 NTAs are shown in Fig. 1. The pattern for the prepared TiO_2 NTAs shows five peaks at 29.53°, 56.54°, 65.08°, 74.48°, and 84.11°, corresponding to (101), (200), (211), (204), and (220) of anatase TiO_2, respectively (ICSD No. 89-4921). In addition to the well-matched diffraction peaks of anatase TiO_2, several peaks in the pattern matched the Ti metals (ICSD No. 89-5009) due to the growth of the thin TiO_2 NTAs on the Ti substrate. Given the low load and the weaker crystallization capacity of 4NBT compared with the TiO_2 NTAs, the diffraction pattern of 4NBT–TiO_2 NTAs has no new diffraction peaks and no peak offset.
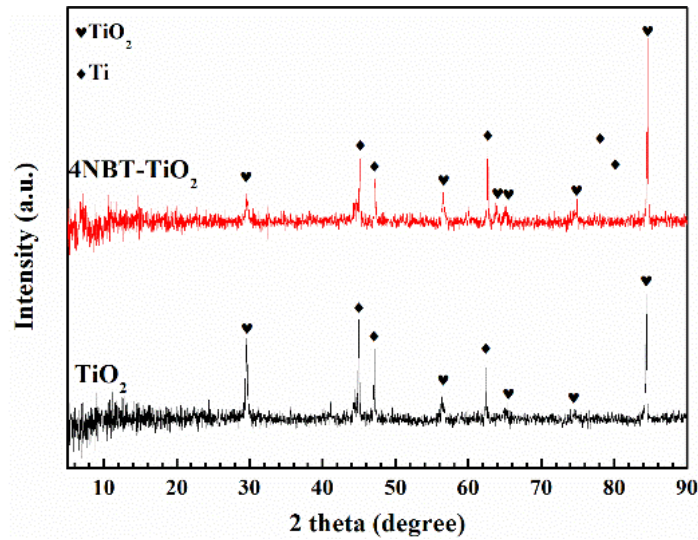
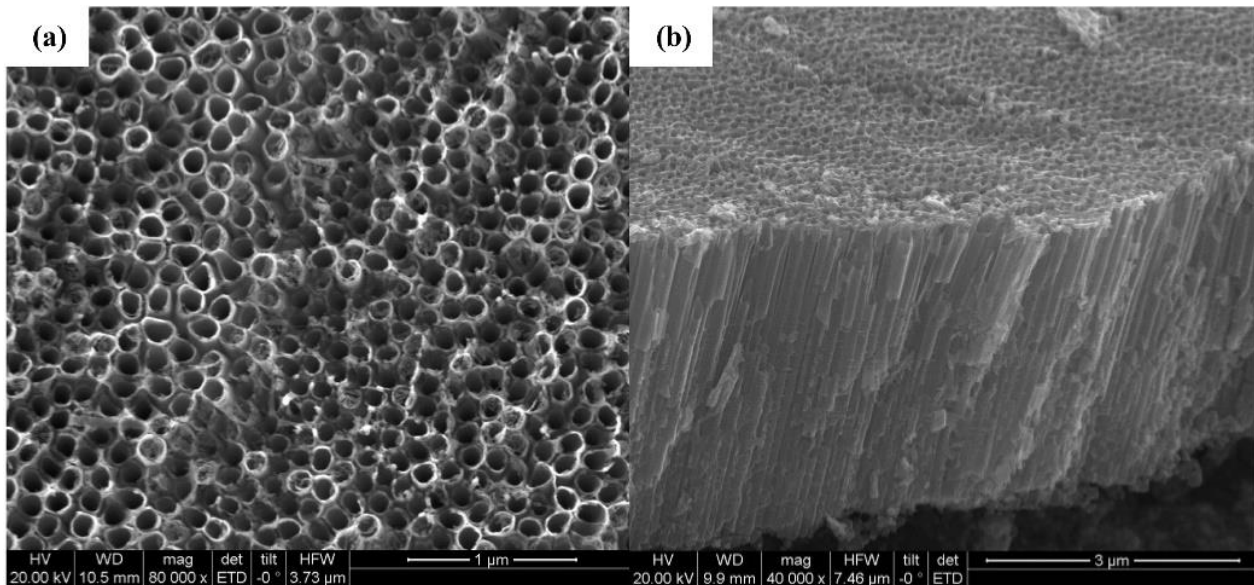**Figure 1.** XRD patterns of the pure TiO$_2$ NTAs and 4NBT–TiO$_2$ NTA$_S$.

Figure 2. (a) top view SEM image of the as-synthesized TiO$_2$ NTAs. (b) cross-sectional view SEM image of the as-synthesized TiO$_2$ NTAs.

The top surface and cross-sectional morphologies of the synthetic sample is shown in Figs. 2a and 2b, respectively. The SEM imaging indicates that the synthetic sample consist of tubes roughly 140 nm in diameters that tend to be vertically oriented and are orderly distributed on the surface of the Ti foil (Fig. 1a). This morphology is consistent with that observed for TiO$_2$ NTAs prepared through a two-step anodization. Fig. 2b reveals that the tubes with length of approximately 320 μm were independent of each other. In addition, bits of fragments can be seen on the cross-sectional morphology because the sample ends to fracture during sample preparation.
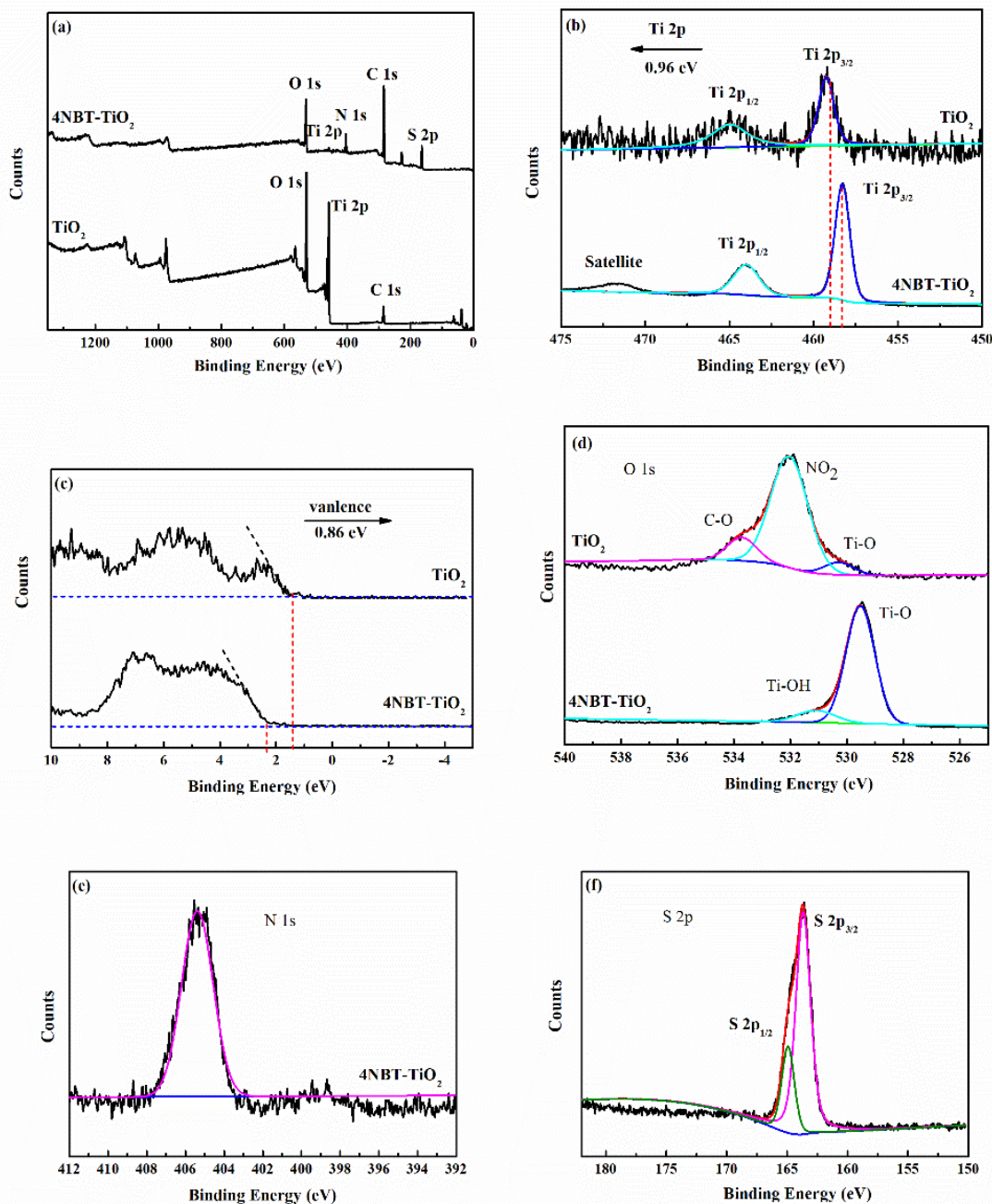
Figure 3. XPS survey, Ti 2p, valence, O 1s, N 1s, and S 2p of the surface of the synthesized 4NBT–TiO$_2$ NTA$_S$.

The element composition and status of the synthesized samples characterized by XPS is displayed in Fig. 3. The XPS results reveal that the elements of the synthesized TiO$_2$ NTAs are Ti and O with C 1s at a binding energy of 284.6 eV as reference spectra (Fig. 3a). Relative to TiO$_2$ NTAs, N and S peaks appear in the XPS of 4NBT–TiO$_2$ NTAs due to the introduction of 4-nitrothiophenol containing N and S. The peak of C is stronger because C is contained in 4NBT–TiO$_2$ NTAs in addition to the exogenous carbon. The weak peak of Ti is due to the introduction of 4-nitrothiophenol, which causes the Ti stray away from the surface. Fig. 3b shows the XPS of Ti in the TiO$_2$ NTAs and 4NBT–TiO$_2$ NTAs. In the spectra of TiO$_2$ NTAs, two symmetric splitting peaks involving satellite features

appear at 458.3 eV with a splitting value of 5.7 eV, which is the typical Ti 2p in TiO_2 [25-26]. In the spectra of 4NBT–TiO_2 NTAs, the binding energy of Ti 2p demonstrated a significant deviation to the higher energy state because the S in 4-nitrothiophenol replaces the O in the surface TiO_2 to form the Ti–S bond. Moreover, the Ti–S bond is strengthened because the conjugate nitro group belongs to the group with strong electron absorption. The variation of valence band is presented in Fig. 3c. The valence band in TiO_2 NTAs (2.40 eV) is formed by the O 2p. When 4-nitrothiophenol was loaded onto the TiO_2 NTAs, the formation of the Ti–S bond caused the valence band to contain O 2p and S 3p (1.54 eV). The negative shift of the valence band will widen the light absorption range. From Fig. 2d, •OH are present on the surface of the TiO_2 NTAs. O in •NO_2 is detected in the XPS of O 1s in the 4NBT–TiO_2 NTAs. In addition, O in organic pollutants is detected, which should be a residual solvent. The peak of N 1s belonging to 4NBT–TiO_2 NTA is at 405.4 eV (Fig. 3e). The formation of the Ti–S bonds, as well as S–C bond with benzene ring, caused the peak of S 2p3/2 at 163.67 eV more positive than metal sulfide (Fig. 3f) [27-29].

The IR spectra of various sample catalysts are shown in Fig. 4. The spectrum of 4NBT–TiO_2 NTAs consists of the characteristic peaks of TiO2 and 4NBT [30-34]. Compared with the IR spectrum of 4NBT, the peak of 4NBT–TiO_2 exhibited some changes. Among them, the υ (C–S) stretching vibration peak located at 675.09 cm^{-1} and the υ (ph–NO_2) stretching vibration peak at 1502.55 cm^{-1} shifted 1.93 and 5.79 cm^{-1}, respectively, toward higher wave numbers. In addition, the sulfhydryl vibration peak, δ (ph–SH), at 2542.18 cm^{-1} in the spectrum of 4NBT–TiO_2 NTAs disappears. In addition, the characteristic stretch peak of Ti–O at 557.43 cm^{-1} in the TiO_2 NTAs spectrum is weakened in the spectrum of 4NBT–TiO_2 NTAs. All changes of the peaks in the above 4NBT–TiO_2 NTAs spectra are caused by the formation of the Ti–S bond between TiO_2 NTAs and 4-nitrothiophenol.
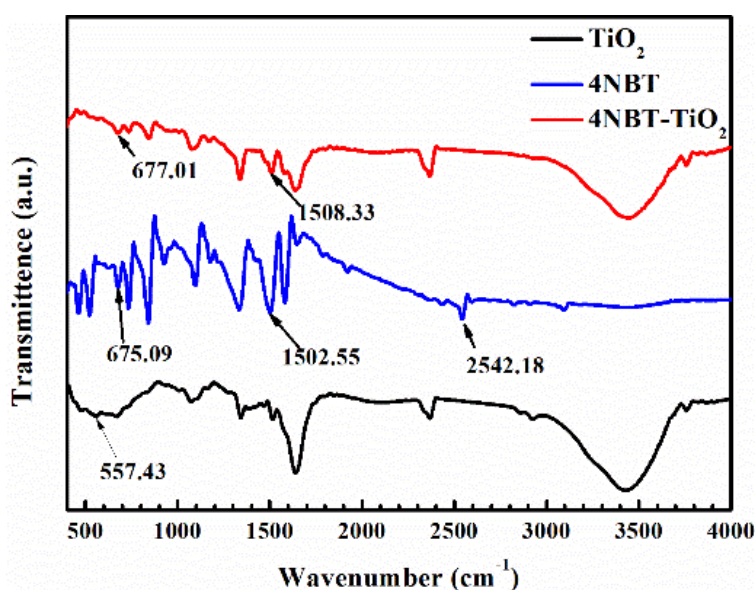

Figure 4. IR spectra of 4NBT, the synthesized TiO_2 NTA$_S$, and 4NBT–TiO_2 NTA$_S$.

The UV–vis DRS of the prepared samples was used to characterize the light absorption property (Fig. 5). Fig. 5a revealed that the prepared TiO_2 NTAs exhibit high absorption intensity in the UV region;

the corresponding absorption band edge is approximately 383.5 nm, which agrees with the property of anatase. Compared to pure TiO_2, 4NBT–TiO_2 NTAs exhibit greater absorption in visible light due to the formation of the Ti–S bond. The formation of Ti-S bond is conducive to the absorption and utilization of solar light by TiO_2 NTAs because the energy proportion of visible light in sunlight is much larger than that of ultraviolet light. The band gap (E_g) of the synthetic samples can be acquired from the $(Ah\upsilon)^2$ vs. $h\upsilon$ plots, where a, h, and υ are the absorbance, Planck constant, and frequency of light, respectively; E_g is the x-intercept of the plots. The E_g of 4NBT–TiO_2 NTAs is 2.72 eV, which is less than that of TiO_2 NTAs (3.22 eV) due to the formation of the Ti–S bond (Fig. 5b). This is due to the valence band in TiO_2 NTAs is formed by the O 2p orbital. When 4-nitrothiophenol was loaded onto the TiO_2 NTAs, the formation of the Ti–S bond caused the valence band to contain O 2p orbital and S 3porbital. The results are consistent with XPS. These results indicate that sensitization with 4NBT can effectively improve the light absorption properties of the TiO_2 NTAs [35-36].
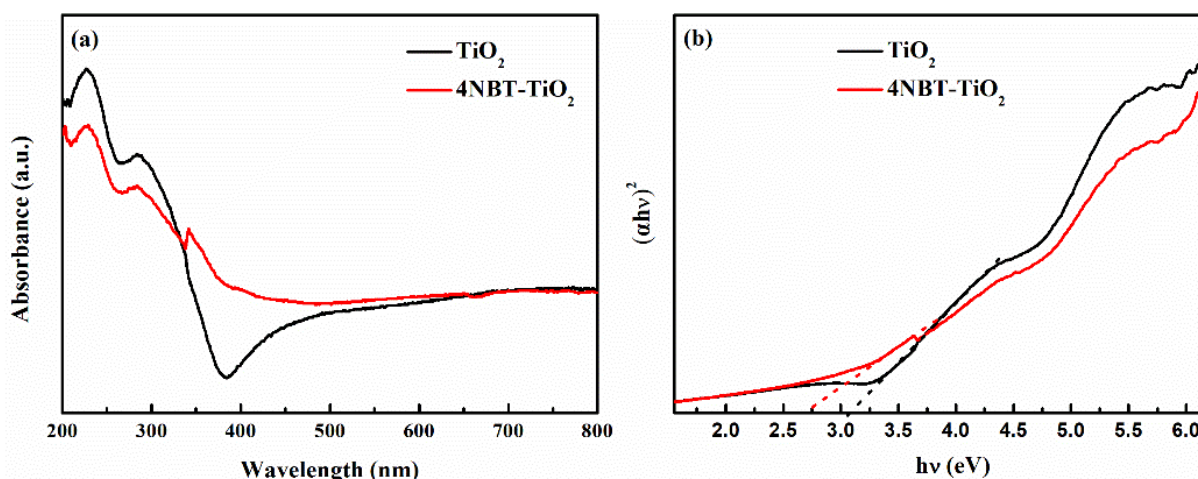

Figure 5. (**a**) UV/Vis diffuse reflectance spectra of the synthesized TiO_2 NTAS and 4NBT–TiO_2 NTAs and (**b**) plots of $(\alpha h\upsilon)^2$ versus hv for TiO_2 NTAS and 4NBT–TiO_2 NTAs.
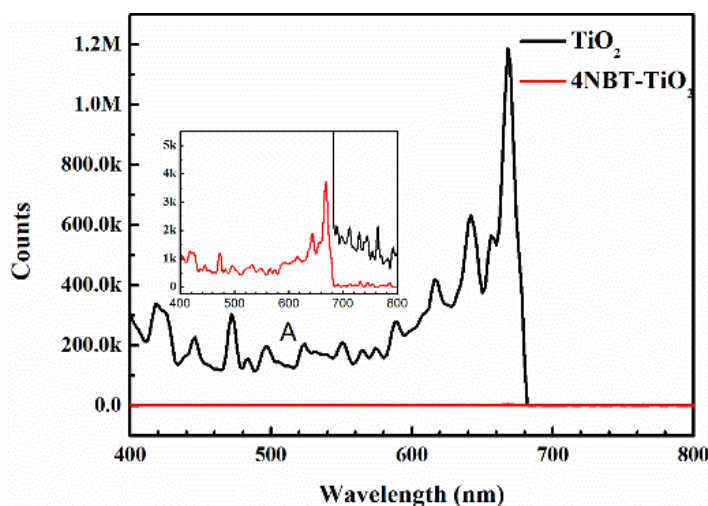

Figure 6. Photoluminescence (PL) spectra of the synthesized TiO_2 NTAs and 4NBT–TiO_2 NTAS with an incident light of 370 nm.

The PL measurements consider the photons emitted from the irradiative recombination of photoinduced electrons and the holes in 4NBT–TiO$_2$ NTAs [37-38]. Thus, the PL spectra of the prepared materials are observed to evaluate the carrier recombination rates (Fig. 6). The same shapes of the two curves indicate that the supported 4NBT did not increase the recombination of photoinduced electrons and holes. The spectral intensity of the 4NBT–TiO$_2$ NTAs is lower than that of pure TiO$_2$. This finding suggests that 4-nitrothiophenol inhibit the recombination of photoinduced carriers in TiO$_2$ NTAs due to the effect of the fast transfer holes of benzene ring, consequently improving the ability of TiO$_2$ NTAs to supply electrons to 304 SS. This will contribute to improving the photocathodic protection performance of TiO$_2$ NTAs.
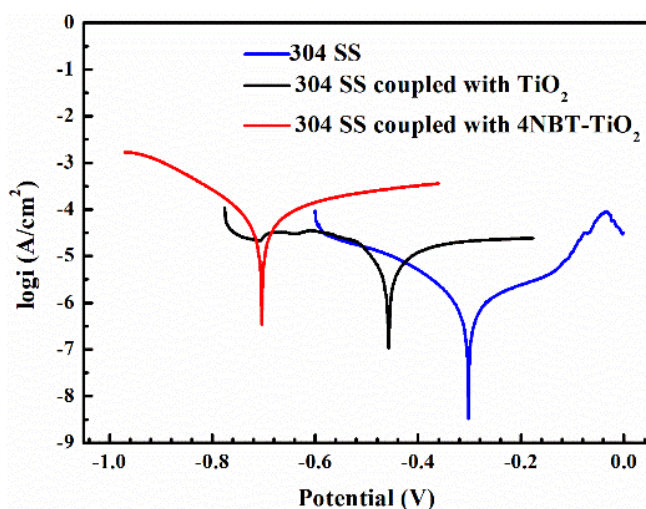

Figure 7. Potentiodynamic polarization curves of 304 SS and 304 SS coupled with the synthesized TiO$_2$ NTAs, 4NBT–TiO$_2$ NTAs.
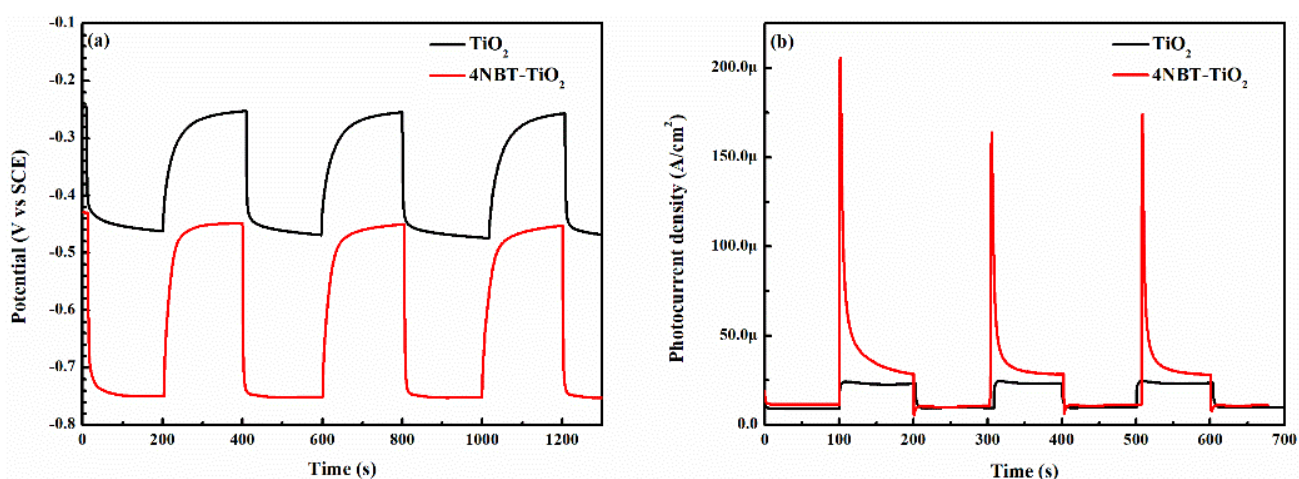

Figure 8. (a) The photoinduced variations of the open circuit potentials and **(b)** variations of the photoinduced current density of the 304 electrode coupled with the synthesized TiO$_2$ NTAs, 4NBT–TiO$_2$ NTAs.

The Potentiodynamic polarization curves of 304 SS with and without photo anode are shown in Fig. 7. The self-corrosion potential of 304 SS in 3.5 wt.% NaCl solution is approximately -300 mv. The

self-corrosion potential exhibited a negative shift when 304 SS was coupled with photo anode under visible light. Because the photoinduced electrons from photo anode under visible light would continue to be transferred to 304 SS, thus replenishing the electrons lost by 304 SS. The 304 SS is protected from corrosion and filled with electrons, with self-corrosion potential shifting negatively. The negative shift of the coupling 4NBT–TiO$_2$ electrode to 304 electrode is the largest. The 304 SS was effectively protected at this potential by inhibiting the dissolution of Fe.

The potential drops of 304 SS coupled with the photoanode and the current densities from 304 SS to the photoanode under visible light characterized the photocathodic protection performance of the prepared photoanode [39]. Fig. 8a shows that when the visible light was switched on, the potential of the 304 electrode coupled with the photoanode dramatically drops due to the large number of electrons induced by the photoanode in visible light. Moreover, the potential drop of the 304 electrode coupled with 4NBT–TiO$_2$ NTAs was 320 mV, which is higher than that coupled with TiO$_2$ NTAs (180 mV). This finding suggests that 4NBT–TiO$_2$ NTAs shows better photocathodic protection performance than TiO$_2$ NTAs. The variation in the current densities of the galvanic couple between the 304 electrode and the prepared photoanode is shown in Fig. 8b. The result reveals that the photo current density of 4NBT–TiO$_2$ NTAs is 28 µA, higher than that of TiO$_2$ NTAs at 20 µA because the formation of the Ti–S bond increases the amount of photoinduced electrons, and the high hole transmission capacity of the benzene ring accelerates the separation of the photogenic carriers. The results are consistent with that of the Potentiodynamic polarization curve.

A mechanism describing the enhanced photocathodic protection performance of the prepared 4NBT–TiO2 NTA electrode is illustrated in Fig. 9. TiO$_2$ NTAs could produce photoinduced charge carriers under visible light exposure. Given the Ti-S bond, The TiO$_2$ NTAs with the assistance of 4-nitrothiophenol can absorb visible light and produce a large number of carriers. The benzene ring in 4NBT could accelerate the transfer of photoinduced carriers. As a result, more photoinduced electrons could be transferred to 304 SS, which inhibits corrosion.
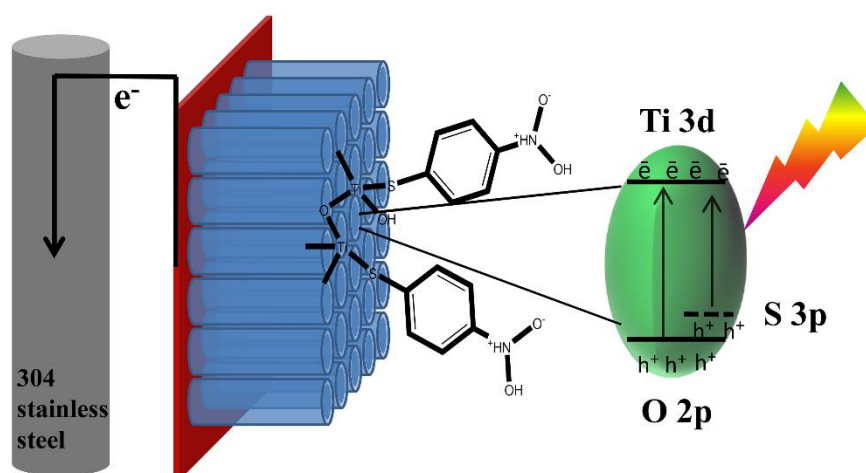

Figure 9. A schematic illustration for the fabrication of the 4NBT–TiO$_2$ NTA$_S$ for photocathodic protection of 304 SS.

4. CONCLUSION

In this study, TiO₂ NTAs were prepared using 4-nitrothiophenol complex on the surface of fabricated arrays via the two-step anodization of Ti substrate, followed by a hydrothermal method. The 4NBT–TiO₂ NTAs exhibited better light absorption and photoinduced carrier separation performance than pure TiO₂, as confirmed by the UV–vis DRS and PL spectrum. The former also displayed better photoelectrochemical performance than TiO₂ NTAs. Furthermore, 4NBT–TiO₂ NTAs can provide great potential for the cathodic protection of 304 SS because of its ability to drop the open circuit potential of 304 SS by 320 mV and provide a current density of 28 µA/cm^2 under visible light illumination, which can effectively protect 304 SS from corrosion.

References

1. B. Hou, X. Li, X. Ma, C. Du, D. Zhang, M. Zheng, W. Xu, D. Lu, and F. Ma, *npj Mater. Degrad*. 1 (2017) 4.
2. J. Yuan, and S. Tsujikawa, *J. Electrochem. Soc*., 142 (1995) 3444.
3. J.J. Zhang, Z.U. Rahman, Y.B. Zheng, C. Zhu, M.K. Tian, and D.A. Wang, *Appl. Surf. Sci*., 457 (2018) 516.
4. S. Masudy-Panah, Y.J.K. Eugene, N.D. Khiavi, R. Katal, and X. Gong, *J. Mater. Chem*. A, 6 (2018) 11951.
5. J. Jing, M. Sun, Z. Chen, J. Li, F. Xu, and L. Xu, *J. Electrochem. Soc*., 164 (2017) C822.
6. J. Azevedo, S.D. Tilley, M. Schreier, M. Stefik, C. Sousa, J.P. Araujo, A. Mendes, M. Gratzel, and M.T. Mayer, *Nano Energy*, 24 (2016) 10.
7. Z. Ma, X. Ma, X. Wang, N. Liu, X. Liu, and B. Hou, *Catalysts*, 9 (2019) 1067.
8. Z. Ma, X. Ma, N. Liu, X. Wang, L. Wang, and B, Hou, *Appl. Surf. Sci.,* 507 (2020) 145088.
9. X. Wang, X. Ning, Q. Shao, S. Ge, Z. Fei, J. Lei, and B. Hou, *Sci. Rep*., 8 (2018) 4116.
10. X. Li, X. Wang, X. Ning, J. Lei, J. Shao, W. Wang, Y. Huang, and B. Hou, *Appl. Surf. Sci*., 462 (2018) 155.
11. J. Low, B. Cheng, and J. Yu, Appl. Surf. Sci., 392 (2017) 658.
12. Q. Liu, Q. Cao, H. Bi, C. Liang, K. Yuan, W. She, Y. Yang, and R. Che, *Adv. Mater.,* 28 (2016) 486.
13. S. Kumar, and K. Rao, Appl. Surf. Sci., 391 (2017) 124.
14. M. Bruening, E. Moons, D.Y. Marcovich, D. Cahen, J. Libman, and A. Shanzer, *J. Am. Chenm. Soc*., 116 (1994) 2972.
15. J. Moser, S. Punchihewa, P. Infelta, and M. Gratzel, *Langmuir.,* 7 (1991) 3012.
16. B. Xu, Y. An, Y. Liu, X. Qin, X. Zhang, D. Wang, P. Wang, M. Whangbo, and B. Huang, *J. Mater. Chem.,* 00 (2017) 1.
17. B. Xu, Y. An, Y. Liu, B. Huang, X. Qin, X. Zhang, Y. Dai, and M. Whangbo, *J. Mater. Chem*., 00 (2017) 1.
18. H. Tsutsumi, S. Furumoto, M. Morita, and Y. Matsuda, *J. Colloid. Interf. Sci*., 171 (1995) 505.
19. D. Nelson, and Z. Schultz, *J. Phys. Chem*. C., 122 (2018) 8581.
20. B. Dong, Y. Fang, L. Xia, H. Xu, and M. Sun, *J. Raman Spectrosc.*, 42 (2011) 1205.
21. B. Dong Y. Fang, X. Chen, H. Xu, and M. Sun, *Langmuir*, 27 (2011) 10677.
22. M. Sun, and H. Xu, *Small,* 8 (2012) 2777.

23. D. Wang and L. Liu, *Chem. Mater.*, 22 (2010) 6656.
24. D. Wang, Y. Liu, B. Yu, F. Zhou, and W. Liu, *Chem. Mater.*, 21 (2009) 1198.
25. W. Gopel, *Surf. Sci.*, 139 (1984) 333.
26. M. Biesinger, L. Lau, A. Gerson, and R. Smart, *Appl. Surf. Sci.*, 257 (2010) 887.
27. Y. Wu, X. Liu, D. Han, X. Song, L. Shi, Y. song, S. Niu, Y. Xie, J. Cai, S. Wu, J. Kang, J. Zhou, Z. Chen, X. Zheng, X. Xiao, and G. Wang, *Nat. Commun.*, 9 (2018) 1425.
28. Y. Fu, C. Zhu, C. Liu, M. Zhang, H. Wang, W. Shi, H. Huang, Y. Liu, and Z. Kang, *Appl. Catal. B-Environ.*, 226 (2018) 295.
29. M. Agostini, J. Hwang, H. Kim, P. Bruni, S. Brutti, F. Croce, A. Matic, and Y. Sun, *Adv. Energy. Mater.*, 8 (2018) 26.
30. Y. Zhang, Y. Hu, G. Li, R. Zhang, *Microchimica Acta*, 186 (2019) 477.
31. C. Ma, Y. Liu, J. Wang, S. Wu, Q. Zhang, P. Soang, L. Xia, *J. Raman Spectrosc.*, 49 (2018) 1395.
32. P. Du, X. Zhang, H. Yin, Y. Zhao, L. Liu, Z. Wu, H. Xu, *Jpn. J. Appl. Phys.*, 57 (2018) 030308
33. Y. Feng, Y. Li, L. Tang, W. Wu, H. Xu, *Tetrahedron Lett,* 51 (2010) 2489.
34. Z. Li, X. Wang, X. Wng, T. Xiao, L. Zhang, P. Lv, and J. Zhao, *Int. J. Hyper.*, 43 (2018) 8859.
35. Z. Wen. N. Wang, J. Wang, B. Hou, *Int. J. Electrochem. Sc.,* 13 (2018) 752.
36. J. Shao, Z. Zhang, X. Wang, X. Zhao, X. Ning, J. Lei, X. Li, B. Hou, J. Electrochem. Soc., 165 (2018) 601.
37. T. Wang, C. Chiang, Y. Lin, V. Srinivasadesikan, M. Lin, Y. Lin, *Appl. Surf. Sci.*, 511 (2010) 145548.
38. C. Hong, H.W. Kim, W.I. Lee, C. Lee, *Thin Solid Films*, 518 (2010) 6638.
39. J. Jing, Z. Chen, Y. Bu, M. Sun, W. Zheng, W. Li, *Electrochim. Acta*, 304 (2019) 386.